

Measurement of the Proton-Air Cross Section with Telescope Array's Black Rock Mesa and Long Ridge Fluorescence Detectors, and Surface Array in Hybrid Mode

R.U. Abbasi,^{1,*} M. Abe,² T. Abu-Zayyad,³ M. Allen,³ R. Azuma,⁴ E. Barcikowski,³ J.W. Belz,³ D.R. Bergman,³ S.A. Blake,³ R. Cady,³ B.G. Cheon,⁵ J. Chiba,⁶ M. Chikawa,⁷ A. di Matteo,^{8,†} T. Fujii,⁹ K. Fujisue,⁷ K. Fujita,¹⁰ R. Fujiwara,¹⁰ M. Fukushima,^{7,11} G. Furlich,³ W. Hanlon,^{3,‡} M. Hayashi,¹² N. Hayashida,¹³ K. Hibino,¹³ R. Higuchi,⁷ K. Honda,¹⁴ D. Ikeda,¹⁵ T. Inadomi,¹⁶ N. Inoue,² T. Ishii,¹⁴ R. Ishimori,⁴ H. Ito,¹⁷ D. Ivanov,³ H. Iwakura,¹⁶ H.M. Jeong,¹⁸ S. Jeong,¹⁸ C.C.H. Jui,³ K. Kadota,¹⁹ F. Kakimoto,¹³ O. Kalashev,²⁰ K. Kasahara,²¹ S. Kasami,²² H. Kawai,²³ S. Kawakami,¹⁰ S. Kawana,² K. Kawata,⁷ E. Kido,⁷ H.B. Kim,⁵ J.H. Kim,¹⁰ J.H. Kim,³ M.H. Kim,¹⁸ S.W. Kim,¹⁸ S. Kishigami,¹⁰ V. Kuzmin,^{20,§} M. Kuznetsov,^{20,8} Y.J. Kwon,²⁴ K.H. Lee,¹⁸ B. Lubsandorzhiev,²⁰ J.P. Lundquist,³ K. Machida,¹⁴ H. Matsumiya,¹⁰ T. Matsuyama,¹⁰ J.N. Matthews,³ R. Mayta,¹⁰ M. Minamino,¹⁰ K. Mukai,¹⁴ I. Myers,³ S. Nagataki,¹⁷ K. Nakai,¹⁰ R. Nakamura,¹⁶ T. Nakamura,²⁵ Y. Nakamura,¹⁶ Y. Nakamura,¹⁶ T. Nonaka,⁷ H. Oda,¹⁰ S. Ogio,^{10,26} M. Ohnishi,⁷ H. Ohoka,⁷ Y. Oku,²² T. Okuda,²⁷ Y. Omura,¹⁰ M. Ono,¹⁷ R. Onogi,¹⁰ A. Oshima,¹⁰ S. Ozawa,²⁸ I.H. Park,¹⁸ M.S. Pshirkov,^{20,29} J. Remington,³ D.C. Rodriguez,³ G. Rubtsov,²⁰ D. Ryu,³⁰ H. Sagawa,⁷ R. Sahara,¹⁰ Y. Saito,¹⁶ N. Sakaki,⁷ T. Sako,⁷ N. Sakurai,¹⁰ K. Sano,¹⁶ T. Seki,¹⁶ K. Sekino,⁷ P.D. Shah,³ F. Shibata,¹⁴ T. Shibata,⁷ H. Shimodaira,⁷ B.K. Shin,³⁰ H.S. Shin,⁷ J.D. Smith,³ P. Sokolsky,³ N. Sone,¹⁶ B.T. Stokes,³ T.A. Stroman,³ T. Suzawa,² Y. Takagi,¹⁰ Y. Takahashi,¹⁰ M. Takamura,⁶ M. Takeda,⁷ R. Takeishi,¹⁸ A. Taketa,¹⁵ M. Takita,⁷ Y. Tameda,²² H. Tanaka,¹⁰ K. Tanaka,³¹ M. Tanaka,³² Y. Tanoue,¹⁰ S.B. Thomas,³ G.B. Thomson,³ P. Tinyakov,^{20,8} I. Tkachev,²⁰ H. Tokuno,⁴ T. Tomida,¹⁶ S. Troitsky,²⁰ Y. Tsunesada,^{10,26} Y. Uchihori,³³ S. Udo,¹³ T. Uehama,¹⁶ F. Urban,³⁴ T. Wong,³ K. Yada,⁷ M. Yamamoto,¹⁶ K. Yamazaki,¹³ J. Yang,³⁵ K. Yashiro,⁶ M. Yosei,²² Y. Zhezher,^{7,20} and Z. Zundel³

(The Telescope Array Collaboraton)

¹*Department of Physics, Loyola University Chicago, Chicago, Illinois, USA*

²*The Graduate School of Science and Engineering, Saitama University, Saitama, Saitama, Japan*

³*High Energy Astrophysics Institute and Department of Physics and Astronomy, University of Utah, Salt Lake City, Utah, USA*

⁴*Graduate School of Science and Engineering, Tokyo Institute of Technology, Meguro, Tokyo, Japan*

⁵*Department of Physics and The Research Institute of Natural Science, Hanyang University, Seongdong-gu, Seoul, Korea*

⁶*Department of Physics, Tokyo University of Science, Noda, Chiba, Japan*

⁷*Institute for Cosmic Ray Research, University of Tokyo, Kashiwa, Chiba, Japan*

⁸*Service de Physique Thorique, Universit Libre de Bruxelles, Brussels, Belgium*

⁹*The Hakubi Center for Advanced Research and Graduate School of Science, Kyoto University, Kitashirakawa-Oiwakecho, Sakyo-ku, Kyoto, Japan*

¹⁰*Graduate School of Science, Osaka City University, Osaka, Osaka, Japan*

¹¹*Kavli Institute for the Physics and Mathematics of the Universe (WPI), Todai Institutes for Advanced Study, University of Tokyo, Kashiwa, Chiba, Japan*

¹²*Information Engineering Graduate School of Science and Technology, Shinshu University, Nagano, Nagano, Japan*

¹³*Faculty of Engineering, Kanagawa University, Yokohama, Kanagawa, Japan*

¹⁴*Interdisciplinary Graduate School of Medicine and Engineering, University of Yamanashi, Kofu, Yamanashi, Japan*

¹⁵*Earthquake Research Institute, University of Tokyo, Bunkyo-ku, Tokyo, Japan*

¹⁶*Academic Assembly School of Science and Technology Institute of Engineering, Shinshu University, Nagano, Nagano, Japan*

¹⁷*Astrophysical Big Bang Laboratory, RIKEN, Wako, Saitama, Japan*

¹⁸*Department of Physics, Sungkyunkwan University, Jang-an-gu, Suwon, Korea*

¹⁹*Department of Physics, Tokyo City University, Setagaya-ku, Tokyo, Japan*

²⁰*Institute for Nuclear Research of the Russian Academy of Sciences, Moscow, Russia*

²¹*Faculty of Systems Engineering and Science, Shibaura Institute of Technology, Minato-ku, Tokyo, Japan*

²²*Department of Engineering Science, Faculty of Engineering,*

Osaka Electro-Communication University, Neyagawa-shi, Osaka, Japan

²³*Department of Physics, Chiba University, Chiba, Chiba, Japan*

²⁴*Department of Physics, Yonsei University, Seodaemun-gu, Seoul, Korea*

²⁵*Faculty of Science, Kochi University, Kochi, Kochi, Japan*

²⁶*Nambu Yoichiro Institute of Theoretical and Experimental Physics, Osaka City University, Osaka, Osaka, Japan*

²⁷*Department of Physical Sciences, Ritsumeikan University, Kusatsu, Shiga, Japan*

²⁸*Quantum ICT Advanced Development Center, National Institute for Information and Communications Technology, Koganei, Tokyo, Japan*

²⁹*Sternberg Astronomical Institute, Moscow M.V. Lomonosov State University, Moscow, Russia*

³⁰*Department of Physics, School of Natural Sciences,*

Ulsan National Institute of Science and Technology, UNIST-gil, Ulsan, Korea

³¹ Graduate School of Information Sciences, Hiroshima City University, Hiroshima, Hiroshima, Japan

³² Institute of Particle and Nuclear Studies, KEK, Tsukuba, Ibaraki, Japan

³³ Department of Research Planning and Promotion, Quantum Medical Science Directorate, National Institutes for Quantum and Radiological Science and Technology, Chiba, Chiba, Japan

³⁴ CEICO, Institute of Physics, Czech Academy of Sciences, Prague, Czech Republic

³⁵ Department of Physics and Institute for the Early Universe, Ewha Womans University, Seodaaemun-gu, Seoul, Korea

Ultra high energy cosmic rays provide the highest known energy source in the universe to measure proton cross sections. Though conditions for collecting such data are less controlled than an accelerator environment, current generation cosmic ray observatories have large enough exposures to collect significant statistics for a reliable measurement for energies above what can be attained in the lab. Cosmic ray measurements of cross section use atmospheric calorimetry to measure depth of air shower maximum (X_{\max}), which is related to the primary particle's energy and mass. The tail of the X_{\max} distribution is assumed to be dominated by showers generated by protons, allowing measurement of the inelastic proton-air cross section. In this work the proton-air inelastic cross section measurement, $\sigma_{p-\text{air}}^{\text{inel}}$, using data observed by Telescope Array's Black Rock Mesa and Long Ridge fluorescence detectors and surface detector array in hybrid mode is presented. $\sigma_{p-\text{air}}^{\text{inel}}$ is observed to be 520.1 ± 35.8 [Stat.] $^{+25.0}_{-40.0}$ [Sys.] mb at $\sqrt{s} = 73$ TeV. The total proton-proton cross section is subsequently inferred from Glauber formalism and is found to be $\sigma_{pp}^{\text{tot}} = 139.4^{+23.4}_{-21.3}$ [Stat.] $^{+15.0}_{-24.0}$ [Sys.] mb.

I. INTRODUCTION

Ultra high energy cosmic rays (UHECRs) offer a unique opportunity as testing grounds for physics beyond the standard model, as they represent a class of particles in the energy frontier beyond what can be generated in human-made accelerators. In addition to questions concerning their astrophysical nature, such as location of sources, composition, acceleration mechanisms, and propagation modes, fundamental aspects regarding the nature of matter can be investigated as well. In particular, UHECRs provide a way to measure the proton interaction cross section at energies beyond what can be achieved in the lab to test standard model predictions of how the cross section evolves with energy beyond what is measured in accelerators. Whereas accelerators are highly controlled environments, specially designed to maximize integrated luminosity, cosmic ray experiments must rely on natural accelerators in the universe which can not be tuned to deliver a desired luminosity. The only choice for UHECR detectors is to increase their aperture to collect more events given a fixed interval of collection time.

UHECR detectors do not directly observe the primary particle of interest due to the extremely low flux of the spectrum ($\sim 10^{-30}$ eV $^{-1}$ m $^{-2}$ sr $^{-1}$ s $^{-1}$) [1]. Instead, the primary particle enters the Earth's atmosphere and quickly interacts with an air molecule generating an extended air shower which generates copious amounts of fluorescence light with secondary particles reaching the ground. Telescope Array collects ~ 3000 events per year

with energies > 1 EeV ($\sqrt{s} > 43$ TeV) with the surface detector array [2], which runs continuously day and night (100% duty cycle), and ~ 700 events per year per each monocular fluorescence detector station [3], which only run on clear, moonless nights ($\sim 10\%$ efficiency), in the same energy range.

In an accelerator experiment cross sections are measured through careful design and control of the source and target, using either colliding beams or fixed target setup. Cross section, σ , in colliding beams is determined by understanding the acceptance of the detector and measuring the event rate for a given beam luminosity, $L = \sigma^{-1} dN/dt$. A cosmic ray measurement of cross section is more akin to a fixed target calorimeter, with the cosmic ray flux acting as the beam and the atmosphere the target material. In the case of UHECRs, the measurement of cross section is made in the lab frame and the atmosphere can be treated as a fixed target since an incoming proton has Lorentz factor γ in excess of 10^9 for $E \geq 1$ EeV. Figure 1 shows the cosmic ray spectrum measured over many decades of energy from the knee to the highest energies observed. The top axis shows the equivalent center of momentum energy of a proton-proton collision of the highest energy terrestrial accelerators. UHECR energies are typically considered as events with $E \gtrsim 1$ EeV ($\sqrt{s} \gtrsim 43$ TeV). As accelerator designs are improved over time, human-made accelerators are closing the energy gap between center of mass energies than can be achieved in the lab and what is provided by nature.

Ultra High Energy Cosmic Ray detectors have been reporting on the proton-air cross section measurement beyond the capability of particle accelerators since 1984 [15–22]. This work presents the second Telescope Array report on the proton-air cross section. The first result was reported in 2015 using the Middle Drum (MD) fluorescence detector and the surface detector in hybrid

* rabbasi@luc.edu

† Currently at INFN, sezione di Torino, Turin, Italy

‡ whanlon@cosmic.utah.edu

§ Deceased

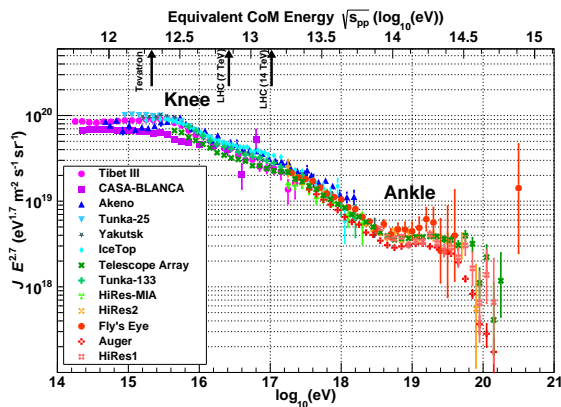


FIG. 1. The cosmic ray spectrum starting at the knee, observed by recent experiments. Cosmic ray energies are measured in the lab frame (i.e., as a fixed target measurement), while the highest energy accelerator based measurements are done using colliding beams, reported in the center of momentum (CoM) frame. Recent accelerator experiments such as the Tevatron and LHC are closing the energy gap between human built accelerators and astrophysical accelerators. Data from [4–14].

mode [23]. In this paper, we are reporting on the inelastic proton-air cross section, at $\sqrt{s} = 73$ TeV, using nearly nine years of data observed by Black Rock Mesa (BRM) and Long Ridge (LR) fluorescence detectors (FDs) and the surface detector (SD) array in hybrid mode. Note that the BRM and LR detectors used in this analysis, are closer in distance than MD to the surface detector array as shown in Figure 2. This enables us to study the inelastic proton-air cross section with higher statistical power for lower energy events. The technique used to analyse these events is similar to that used in the first proton-air cross section report [23]. The statistical power, on other hand, increased by a factor of four. Note that all the systematic sources are revisited and updated in addition to using the most recent hadronic high energy models.

The proton-proton cross section is also calculated in this work using Glauber formalism [24] and BHS fit [25]. The inelastic proton-air and the total proton-proton cross section are compared to previous cosmic ray experimental results and to predictions from models.

II. DETECTOR DESCRIPTION

Telescope Array (TA) is a cosmic ray observatory that deploys multiple types of detectors to record the passage of extended air showers caused by ultra high energy cosmic ray primaries as they impact in the Earth's atmosphere. The primary way TA observes air showers is by using surface detectors which detect the energy deposited by high energy particles as they pass through them or using fluorescence detectors which observe the UV light generated in the atmosphere as the shower particles interact and exchange energy with air molecules. SDs do

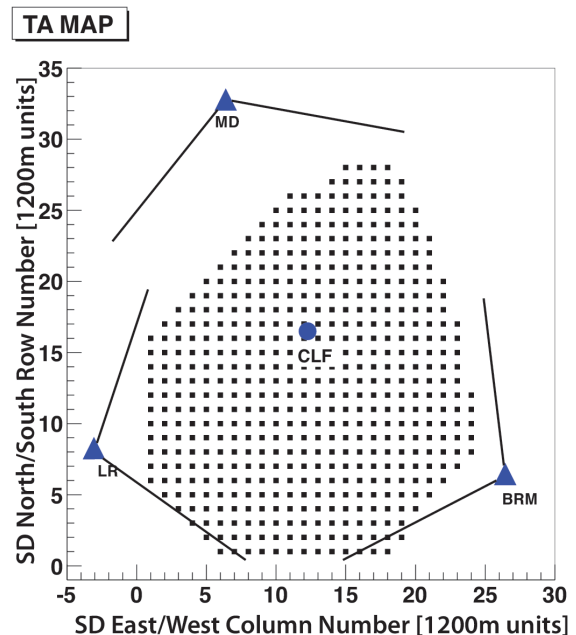


FIG. 2. The Telescope Array detector configuration. The filled squares are the 507 SD scintillators on a 1.2 km grid. The SD scintillators are enclosed by three fluorescent detectors shown in filled triangles together with their field of view in solid lines. The northernmost fluorescence detector is called Middle Drum while the southern fluorescence detectors are referred to as Black Rock Mesa and Long Ridge. The filled circle in the middle equally spaced from the three fluorescence detectors is the Central Laser Facility used for atmospheric monitoring and detector calibration.

not measure the development of the air shower in the sky, while FDs do. The shower size, number of charged particles at depth X ($N(X)$), of an air shower can be parameterized using the Gaisser-Hillas function [26]

$$N(X) = N_{\max} \left(\frac{X - X_0}{X_{\max} - X_0} \right)^{\frac{X_{\max} - X_0}{\lambda}} \exp \left(-\frac{X_{\max} - X}{\lambda} \right) \quad (1)$$

where N is the number of particles at slant depth X . The parameters N_{\max} , X_{\max} , X_0 , and λ describe the shower shape. N_{\max} is the maximum number of shower particles and the slant depth at which this occurs is denoted by X_{\max} . λ and X_0 correspond to the proton-air interaction length and slant depth of first interaction, respectively.

In practice, when fitting real shower profiles using the Gaisser-Hillas function, λ and X_0 are fixed parameters, while X_{\max} is observed by the FDs. To get an accurate measure of X_{\max} , a monocular FD measurement is not sufficient. To improve X_{\max} resolution, simultaneous observation of a shower by multiple FD stations must be employed or simultaneous observation by a FD station and the SD ground array. In the case of multiple FD stations, the independently measured shower-detector planes provide a strong constraint on the shower track, leading to greatly improved geometrical resolu-

tion. Similarly, a shower observed by a single FD station, along with the arrival time and core location on the ground provided by the SD array delivers the same benefit. Resolution on X_{\max} improves dramatically from 84 and 52 g/cm² for showers with energies of 1 EeV to 100 EeV respectively [27] to ~ 20 g/cm² for $E > 1$ EeV when using multiple sets of observing stations to record showers.

Telescope Array is located in central Utah's Millard County, USA. The SD ground array is composed of 507 plastic scintillator counters spread over 700 km². The center of the SD array is located at 39° 17' 49"N 112° 54' 31"W, 1370 masl. Three FD stations overlooking the SD array are located outside the array boundary. All FD stations are located ~ 21 km away from the center of the SD array. Middle Drum station is located on the north end of the array, Black Rock Mesa is located at the south-east border and Long Ridge is located at the southwest border. This work uses FD data from the Black Rock Mesa and Long Ridge detectors. While the general operation of all FDs is similar, the design and location of the Middle Drum detector relative to the SD array border results in different low energy acceptance than the Black Rock Mesa and Long Ridge detectors. The description of FD equipment used in this analysis that follows is for Black Rock Mesa and Long Ridge.

Each FD station is comprised of twelve telescopes consisting of a multi-segmented 6.8 m² mirror, a 16x16 photomultiplier tube (PMT) array camera, electronics to digitize PMT signals at 40 MHz, trigger on air shower track candidates, and readout and communications with a remote DAQ which controls event readout and storage among all of the electronics racks. The telescopes are arranged in a two ring configuration providing zenith angle coverage in two bands. Six telescopes are assigned to ring 1, observing 3° – 17° in elevation angle and six are assigned to ring 2 observing 17° – 31°. Azimuthal coverage of 108° is the same for both rings. On clear, moonless nights the FDs scan the skies for potential air shower events. Because of this constraint, FD collection efficiency is about 10%, whereas properly operating SDs have 100% operating efficiency since SDs can operate in all weather conditions 24 hours a day. Each FD electronics rack has a track finder module which implements temporal-spatial pattern recognition algorithms to determine if a track has been observed. If a set of tube triggers meets the criteria an event level trigger is generated and communicated to the remote DAQ which forces readout of all mirrors for storage and offline analysis. BRM and LR electronics utilize FADC electronics which allows digitization of PMT signals at an equivalent 14-bit, 10 MHz sampling rate, allowing observation of the time development of an event with 100 ns time resolution. Above 10^{18.2} eV, showers are seen with distance of closest approach (impact parameter) > 25 km. Further details about the construction and design of the BR and LR stations can be found in [28, 29].

Each surface detector is composed of two layers of 3 m²

plastic scintillator, 1.2 cm thick. Wavelength shifting fibers are embedded in grooves in the scintillator layers and optically coupled to a PMT (one for each layer). PMT signals are digitized by a 12 bit FADC operating at 50 MHz sampling rate. Onboard electronics deployed with each SD scan for signals above threshold (> 3 minimum ionizing particles) and generate a trigger for signals that exceed this level. These triggers are relayed to one of three remote DAQ stations by wireless radio communications. The remote DAQ stations are responsible for generating event level triggers based upon simple temporal-spatial pattern matching. When a sufficient number of SDs submit triggers that meet the criteria for an event level trigger, the remote DAQ station broadcasts a directive for all SDs that observed signal above a threshold to readout (> 0.3 minimum ionizing particles) and send their data to the DAQ for storage and offline analysis. SDs are placed in a grid-like manner, with separation distance of 1.2 km. SD array event reconstruction efficiency saturates at 10^{18.9} and becomes 100% efficient with no zenith angle dependence. Refer to [30] for further information regarding the technical details of TA's surface detector array.

The second additional cut added to this analysis is a zenith angle cut. Because the atmosphere acts as a calorimeter, fluorescence detectors are limited in their ability to reconstruct showers based upon the atmospheric overburden available for air showers to develop. Fluorescence detectors far above sea level in general will accept fewer showers for reconstruction than those closer to sea level, because the higher detector has less atmosphere for the shower to reach maximum size before hitting the ground. Thus, showers with small zenith angle (close to vertical) traverse less atmosphere than those with large zenith angle, reducing the chance that the shower will achieve maximum size before penetrating the ground or falling below the field of view of the detector. Figure 4 shows Telescope Array hybrid X_{\max} acceptance of QGSJET II.4 protons. As seen in the figure, events with zenith angle less than 30 degrees show a break in acceptance roughly corresponding to the vertical depth of ground level, indicated by the dashed line showing the vertical depth of the Central Laser Facility (CLF) at the center of the SD array. Events that have zenith angle greater than 30 degrees, are sufficiently inclined to provide enough slant depth to reach shower maximum in the atmosphere. Indeed, these events show no significant break in the X_{\max} acceptance.

The proton-air cross section measurement uses information from the deep tail of the X_{\max} distribution under the assumption that only light primaries such as protons, and possibly some helium contamination, populate this region of the distribution. To ensure the highest level of proton purity in the tail of the X_{\max} distribution used to determine $\sigma_{\text{p-air}}^{\text{inel}}$, we search for the minimum zenith angle cut which results in nearly flat X_{\max} acceptance for all X_{\max} in the energy range $18.2 \leq \log_{10}(E/\text{eV}) < 19.0$. If X_{\max} acceptance shows a break in the deep X_{\max} re-

gion for some range of zenith angles, those events must be removed because showers induced by proton primaries may be lost in the X_{\max} distribution tail.

Analysis, data, and Monte Carlo used for this work is identical to that used in [31] except for energy binning and the additional zenith angle cut described above. The resultant data set contains 1975 events with a resolution in X_{\max} of ~ 20 g/cm² and an average energy of $10^{18.45}$ eV. For further details concerning the hybrid analysis procedure refer to [31].

III. DATA TRIGGER, RECONSTRUCTION, AND SELECTION.

The FD and SD data streams are collected independent of each other. To create a hybrid data stream the streams are searched for coincident triggers that occur within 500 μ s. For this set of hybrid events, SD reconstruction proceeds as described in [30] to determine the shower core location and arrival time. FD reconstruction is performed as described in [3] to determine the shower-detector plane for each FD station that observes a shower. This determines the shower-detector plane angle, ψ , impact parameter, core location, and arrival time. A hybrid reconstruction takes the additional step of casting the individual SDs into “pixels” that observe the shower in a similar way FD PMTs do. This allows us to use them in the shower-detector plane fit. Because of their accurate measure of the shower track position and arrival time on the ground, these points provide an additional constraint on the track geometry. Once the hybrid shower geometry is determined, the shower profile is measured by each observing FD station using this improved measure of the shower track. Shower profile reconstruction determines the shower size measured by the number of charged particles as a function of atmospheric depth (equation 1) and proceeds as described in [3]. The shower profile is used to determine the primary particle energy and X_{\max} , both of which are the essential inputs to the proton-air cross section measurement.

The data used for this analysis was collected from 2008 May 27 to 2016 November 29, nearly nine years, and is the same data used the BR/LR hybrid X_{\max} measurement in [31]. That analysis examined X_{\max} for events with $E \geq 10^{18.2}$ eV and resulted in 3330 events after applying all quality cuts to the data. The present analysis imposes two more cuts on the data required for a good quality cross section measurement: here we restrict analysis to events with energy $18.2 \leq \log_{10}(E/\text{eV}) < 19.0$ and zenith angle $> 30^\circ$. The rationale for these additional cuts is described below.

Abbasi *et al.* [31] demonstrated that below $10^{19.0}$ eV, the TA RMS of the X_{\max} distribution $\sigma(X_{\max})$ is consistent with light composition ranging between 52 and 63 g/cm². Above this energy $\sigma(X_{\max})$ begins to decrease. Due to changing zenith angle acceptance and falling statistics it is premature to say if this narrowing

of $\sigma(X_{\max})$ is astrophysical in nature or caused by selection bias. We can compare TA’s observed mean $\langle X_{\max} \rangle$ and RMS $\sigma(X_{\max})$ of the X_{\max} distribution to Monte Carlo predictions by randomly sampling the X_{\max} distributions of individual elements such as proton, helium, nitrogen, and iron according to data statistics. To do this the simulated X_{\max} distributions of each of those elements is randomly sampled N times, where N is the number of events observed in the data for the given energy bin, a distribution of X_{\max} is therefore generated, and $\langle X_{\max} \rangle$ and $\sigma(X_{\max})$ of the distribution is recorded. Note that the X_{\max} distributions are fully simulated with all acceptance effects present in reconstructed data. This procedure is repeated 5000 times. We can then measure the 68%, 90%, and 95% confidence intervals of the joint expectation of $\langle X_{\max} \rangle$ and $\sigma(X_{\max})$ for each element as shown. We can then compare the predictions of $\langle X_{\max} \rangle$ and $\sigma(X_{\max})$ to what is observed in the data, which is shown in figure 3 for two energy bins. The figure also shows $\langle X_{\max} \rangle$ and $\sigma(X_{\max})$ observed by TA, as well as the systematic and statistical uncertainties.

Figure 3a shows $\langle X_{\max} \rangle$ and $\sigma(X_{\max})$ observed for $18.2 \leq \log_{10}(E/\text{eV}) < 18.3$ and the predictions for primary particle spectra of pure proton, helium, nitrogen and iron using the QGSJET II.4 hadronic model. This is the lowest energy bin used and the one with the most statistics (801 events) in that analysis. $\langle X_{\max} \rangle$ and $\sigma(X_{\max})$ of the data are closest to the prediction of QGSJET II.4 protons. Additionally, the predictions from Monte Carlo simulation have relatively small dispersion and are easily distinguishable because of the relatively large statistics in this energy bin. The TA hybrid data is tested against these single element models and, in this energy bin, it is easy to see given TA’s statistical and systematic errors, as well as the clear separation in simulated $\langle X_{\max} \rangle$ and $\sigma(X_{\max})$, that the best fit to the data is compatible to only one element within systematic errors. The situation changes though where statistics are small, as shown in figure 3b. This energy bin shows $\langle X_{\max} \rangle$ and $\sigma(X_{\max})$ observed for $19.4 \leq \log_{10}(E/\text{eV}) < 19.9$ as well as the single element predictions. It only has 19 events and is the lowest statistics bin in that analysis, with statistical power falling due to the competing effects of a steeply falling primary particle spectrum and zenith angle acceptance of hybrid reconstruction. Compared to figure 3a, observed $\langle X_{\max} \rangle$ here has increased as predicted due to the relationship between primary particle energy and X_{\max} and observed $\sigma(X_{\max})$ has decreased. But the simulations predict much larger dispersion in the $\langle X_{\max} \rangle$ and $\sigma(X_{\max})$, causing the data to be indistinguishable from light single element models such as proton, all the way up to single element nitrogen. Above $E \geq 10^{19.0}$ eV the observed data exhibits this effect to such a degree that we impose an additional cut eliminating events above this energy for the present analysis to ensure that the tail of the X_{\max} distribution used for the p-air cross section measurement is not significantly contaminated with heavy elements. We also estimate the

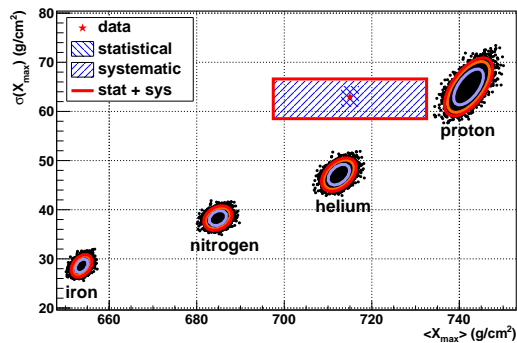
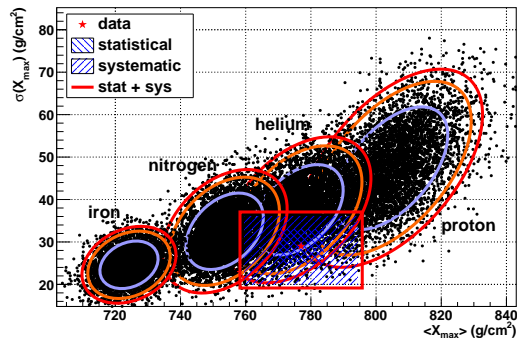
(a) $18.2 \leq \log_{10}(E/\text{eV}) < 18.3$ (b) $19.4 \leq \log_{10}(E/\text{eV}) < 19.9$

FIG. 3. Measurements of data and QGSJet II.4 Monte Carlo $\langle X_{\max} \rangle$ and $\sigma(X_{\max})$ in energy bins for $18.2 \leq \log_{10}(E/\text{eV}) < 18.3$ and $19.4 \leq \log_{10}(E/\text{eV}) < 19.9$. The star represents $\langle X_{\max} \rangle$ and $\sigma(X_{\max})$ observed by TA in the two energy bins, as well as the statistical and systematic uncertainties. Each Monte Carlo chemical element shows the 68.3% (blue ellipse), 90% (orange ellipse), and 95% (red ellipse) confidence intervals.

contamination in the tail due to helium and this estimate is described later in this section.

The second additional cut added to this analysis is a zenith angle cut. Because the atmosphere acts as a calorimeter, fluorescence detectors are limited in their ability to reconstruct showers based upon the atmospheric overburden available for air showers to develop. Fluorescence detectors far above sea level in general will accept fewer showers for reconstruction than those closer to sea level, because the higher detector has less atmosphere for the shower to reach maximum size before hitting the ground. Thus, showers with small zenith angle (close to vertical) traverse less atmosphere than those with large zenith angle, reducing the chance that the shower will achieve maximum size before penetrating the ground or falling below the field of view of the detector. Figure 4 shows Telescope Array hybrid X_{\max} acceptance of QGSJET II.4 protons. As seen in the figure, events with zenith angle less than 30 degrees show a break in acceptance roughly corresponding to the vertical depth of ground level, indicated by the dashed line showing the vertical depth of the Central Laser Facility (CLF) at the center of the SD array. Events that have zenith angle

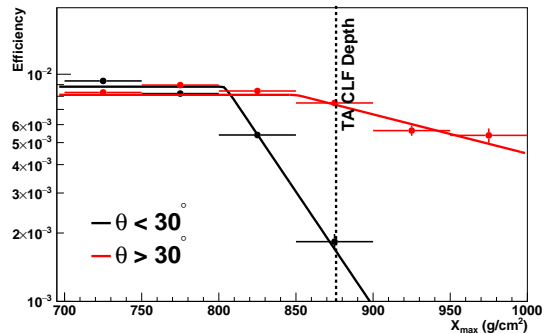


FIG. 4. Telescope Array hybrid QGSJET II.4 proton X_{\max} acceptance in two zenith angle bands for energies $18.2 \leq \log_{10}(E/\text{eV}) < 19.0$. The black shows the reconstruction efficiency of events with zenith angle < 30 degrees and red line is the efficiency with zenith angle > 30 degrees. Small zenith angle events are more likely to achieve shower maximum below the FD field of view and therefore the acceptance drops roughly at the vertical depth of ground level at TA. The dashed line shows the vertical depth of the TA Central Laser Facility (CLF). Inclined events with large zenith angle are more likely to reach shower maximum in the atmosphere and the acceptance does not significantly fall off with slant depth.

greater than 30 degrees, are sufficiently inclined to provide enough slant depth to reach shower maximum in the atmosphere. Indeed, these events show no significant break in the X_{\max} acceptance.

The proton-air cross section measurement uses information from the deep tail of the X_{\max} distribution under the assumption that only light primaries such as protons, and possibly some helium contamination, populate this region of the distribution. To ensure the highest level of proton purity in the tail of the X_{\max} distribution used to determine $\sigma_{\text{p-air}}^{\text{inel}}$, we search for the minimum zenith angle cut which results in nearly flat X_{\max} acceptance for all X_{\max} in the energy range $18.2 \leq \log_{10}(E/\text{eV}) < 19.0$. If X_{\max} acceptance shows a break in the deep X_{\max} region for some range of zenith angles, those events must be removed because showers induced by proton primaries may be lost in the X_{\max} distribution tail.

Analysis, data, and Monte Carlo used for this work is identical to that used in [31] except for energy binning and the additional zenith angle cut described above. The resultant data set contains 1975 events with a resolution in X_{\max} of ~ 20 g/cm² and an average energy of $10^{18.45}$ eV. For further details concerning the hybrid analysis procedure refer to [31].

IV. ANALYSIS

The proton-air inelastic cross section σ is related to interaction length λ (mean free path) by

$$\lambda = 1/(n\sigma) \quad (2)$$

where n is the target particle density. The probability of an interaction in a slab of target material of thickness dx is $P(x) = (1/\lambda)dx$. Given a “beam” of cosmic rays, beam intensity, I , decreases with increasing number of slabs traversed as $dI = -I/\lambda dx$, leading to the expression of beam intensity, $I(x) = I_0 \exp(-x/\lambda)$, where I_0 is the initial intensity and x is depth. Therefore for cosmic rays the interaction length can be measured by fitting a distribution of depth of first interaction (X_0) between the cosmic ray primary particle and an air nucleus to find λ . In practice this is not feasible because the starting point of the upper atmosphere is not well defined due to its very low density and there is no appreciable fluorescence signal generated at first interaction.

After the initial inelastic collision an air shower continues to grow in size through production of secondaries mainly by radiative processes of pair production and bremsstrahlung in the electromagnetic portion of the shower. The shower grows until it reaches a maximum size, X_{\max} , dependent primarily on primary particle energy and mass, then decreases as energy loss of secondaries becomes dominated by collisional processes. X_{\max} therefore is a uniquely defined point in the shower profile that is observed by fluorescence detectors and can be used as a proxy for X_0 to determine the interaction length of a distribution of cosmic ray primaries. Proton-air cross section is therefore measured indirectly for air showers.

In this work, the *K-Factor method* [23] is used to obtain the proton-air cross section. The tail of the X_{\max} distribution retains the exponentially falling nature of the X_0 distribution encoded within it and can be parameterized as $f(X_{\max}) = \exp(-X_{\max}/\Lambda_m)$, where Λ_m is the exponential slope of the tail. The *K-Factor method* relates the slope of the tail of the X_{\max} distribution and to the slope of X_0 distribution, through a constant factor K which is determined by MC simulation and is close to unity.

$$\Lambda_m = K \lambda_{p-\text{air}} \quad (3)$$

where we now label $\lambda_{p-\text{air}}$ as the proton-air interaction length and both Λ_m and $\lambda_{p-\text{air}}$ are measured in g/cm^2 . Using the relationship between λ and σ expressed in equation 2, cross section can be related to the mean target mass of air as

$$\sigma_{p-\text{air}}^{\text{inel}} = \frac{\langle m_{\text{air}} \rangle}{\lambda_{p-\text{air}}} \quad (4)$$

and substituting this into equation 3 we find

$$\Lambda_m = K \frac{24160}{\sigma_{p-\text{air}}} = K \frac{14.45 m_p}{\sigma_{p-\text{air}}} \quad (5)$$

where $\langle m_{\text{air}} \rangle = 24160 \text{ mb g cm}^{-2}$ or $14.45 m_p$ with the proton mass expressed in g [32]. $\sigma_{p-\text{air}}^{\text{inel}}$ is expressed in mb and Λ_m is in g/cm^2 . This equation directly links the observed X_{\max} distribution to the proton-air cross section.

This *K-Factor method* is the same method used in the first TA report on the proton-air cross section in 2015 [23]. The data analysis here is divided into two parts. The first part is done by calculating the value of the attenuation length (Λ_m) of the observed UHECR events. In the second part, we calculate the inelastic proton-air cross section ($\sigma_{p-\text{air}}^{\text{inel}}$) value from the obtained attenuation length Λ_m .

A. Measuring the Attenuation Length Λ_m

The value of attenuation length Λ_m , and therefore the proton-air cross section, can be calculated by fitting the X_{\max} distribution tail to the exponential function $\exp(-X_{\max}/\Lambda_m)$. Here only the tail of the X_{\max} distribution is used to obtain Λ_m , because it is the most penetrating part of the distribution and is assumed to be composed mostly of protons. UHECR composition can not be measured on an event by event basis and must be inferred from a distribution of events. By restricting the determination of Λ_m to the tail of the X_{\max} distribution, potential contamination from heavier elements in the primary spectrum is reduced.

The choice of the starting point of the tail fit (the lower edge of the fit range) X_i for the exponential fit is made by fitting the X_{\max} distribution tail to two exponential functions with separate power indices. The break point of these two fits (found to be at $790 \text{ g}/\text{cm}^2$) describe the best fit beyond which the distribution can be described using a single exponential function. This maximizes the number of events in the tail distribution while minimizing instability in the value of Λ_m due to possible detector bias or helium contamination.

Figure 5 shows the X_{\max} distribution of the data collected by the Telescope Array southern most fluorescence detectors, Black Rock Mesa and Long Ridge, together with the surface detector hybrid events. The distribution includes 1975 events in the energy range between $10^{18.2} - 10^{19.0} \text{ eV}$ with an average energy of $10^{18.45} \text{ eV}$. The data included here passed the quality cuts described in the previous section and is fitted to the exponential function $\exp(-X_{\max}/\Lambda_m)$ using the unbinned maximum likelihood method.

Several systematic checks are applied to test for the stability of the measured attenuation length Λ_m . This is done by dividing the data in two halves based on: the zenith angle, the distance of the shower using the impact parameter R_p , and the energy of the event. The divided subsets are found to be consistent within statistical fluctuations.

The final Λ_m measured by the Telescope Array detector at an average energy of $10^{18.45} \text{ eV}$ ($\sqrt{s} = 73 \text{ TeV}$) including the statistical checks is found to be $\Lambda_m = 55.9 \pm 3.8 [\text{Stat.}] \text{ g}/\text{cm}^2$. Note that Λ_m is directly derived from the data and is model independent. Therefore, it can be used at a later time to calculate the inelastic proton-air cross section independent of the method or the UHECR

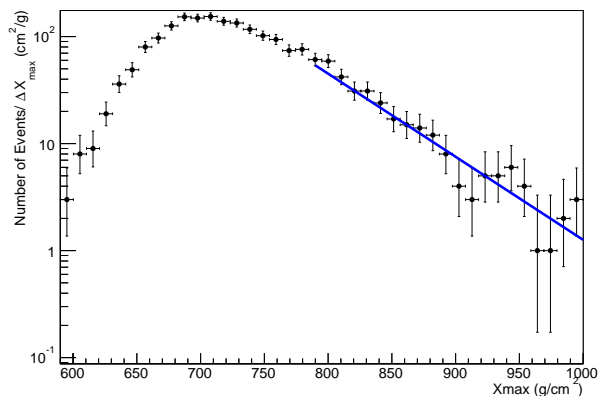


FIG. 5. The number of events per X_{\max} bin (ΔX_{\max}) vs. X_{\max} g/cm² for BRM and LR fluorescence detectors and the Telescope Array surface detector in hybrid mode. The line is the exponential fit to the slope using the unbinned likelihood method between 790-1000 g/cm².

models used in this paper.

B. Proton-Air cross Section Measurement

To determine the interaction mean free path of protons in air, $\lambda_{p-\text{air}}$ and therefore the inelastic proton-air cross section $\sigma_{p-\text{air}}^{\text{inel}}$ we use the K -Factor technique. Using equation 3, K can be directly computed using Monte Carlo. K depends on the hadronic model being used in simulations. UHECR simulations rely on the choice of electromagnetic interaction driver, low energy hadronic generator, and high energy hadronic generator [33]. The most popular high energy hadronic generators are SIBYLL2.3 [34, 35], EPOS-LHC [36], QGSJET II.4 [37, 38], and QGSJET01 [39] which, with the exception of QGSJET01, are tuned to the most recent accelerator data at energies accessible to accelerators and extrapolated to UHECR energies through theoretical and phenomenological predictions. Hadronic model dependence is an important and difficult consideration when dealing with questions related to the fundamental properties of hadronic air showers such as proton-air cross section or cosmic ray composition. Some of the important parameters that affect shower development which are extrapolated from accelerator data to UHECR energies are inelasticity, multiplicity, and cross section. Each

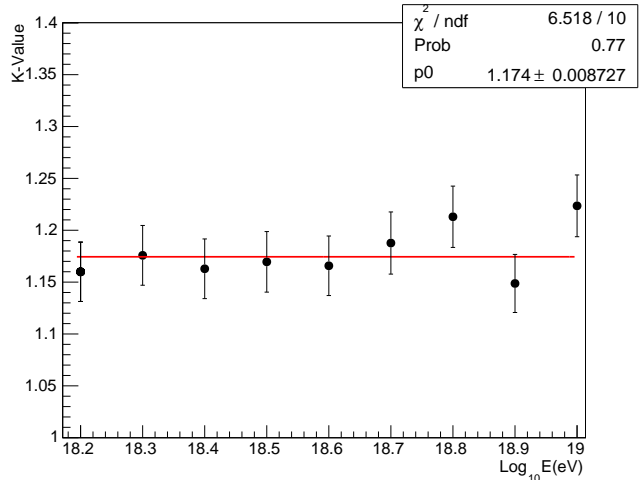


FIG. 6. The value of K obtained vs. energy in $\text{Log}_{10}(\text{eV})$ for simulated data sets using CONEX 6.4 with the high energy model QGSJET II.4, for the energy range of the data, between $10^{18.2}$ and $10^{19.0}$ eV.

hadronic generator uses different methods to do this leading to differences in shower development at ultra high energies. For a summary of these issues refer to [40, 41]. For this work we present the results for several different models and report on the systematic uncertainty in the results of our measurement.

K is computed in this work by generating several simulated sets between $10^{18.2} - 10^{19}$ eV for each of the high energy models. Each generated set contains ten thousand events using a one-dimensional air shower Monte Carlo program CONEX 6.4 [42–44]. Figure 6 shows the K -value including the statistical fluctuation calculated for each of these simulated sets, using QGSJET II.4 as an example. The value of K is then obtained by fitting the K -value vs. energy to a horizontal line as shown in Figure 6. It is important to note that the value of Λ_m and therefore, the value of K is dependent on the choice of the lower edge of the tail fit range X_i (as shown in Figure 7). A consistent procedure needs to be used to determine X_i and therefore the value of K for each energy bin and the high energy model shower simulations. To do so we calculate the difference in slant depth D between the peak of the X_{\max} distribution and 790 g/cm², using a simulated data set at an energy of $10^{18.45}$ eV (equivalent to the mean energy of the data set used in this work). The same difference in slant depth D is later used to consistently determine the value of X_i from peak of the X_{\max} distribution for each of the simulated sets for each of the high energy models.

To confirm the validity of the obtained K values, for each of the generated data sets, for each of the high energy models, $\lambda_{p-\text{air}}$ is reconstructed and compared to the $\lambda_{p-\text{air}}$ provided by the corresponding high energy model. Figure 8 shows the comparison of the values of the high energy model $\lambda_{p-\text{air}}$ and the obtained $\lambda_{p-\text{air}}$ using

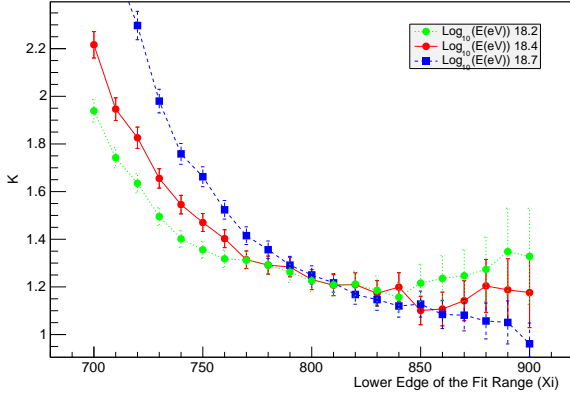


FIG. 7. The value of K vs. the lower edge in the fit range (X_i) to the tail of the X_{\max} distribution for several data sets $10^{18.2}$, $10^{18.4}$, and $10^{18.7}$ eV simulated using CONEX with the high energy model QGSJET II.4. Each data set contains 10,000 simulated events.

the K -Factor technique. Figure 8 shows that the value of K obtained in this study indeed describes the value of K of the high energy models correctly.

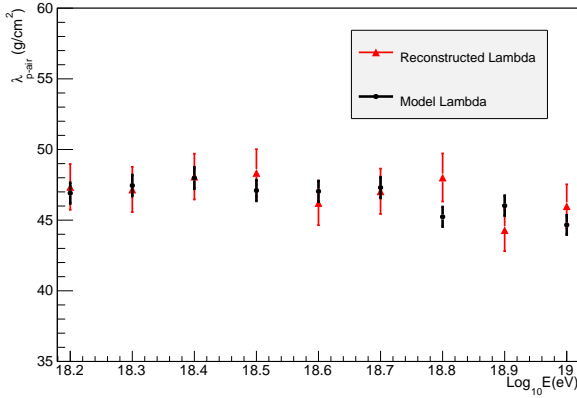


FIG. 8. The proton-air interaction length $\lambda_{p\text{-air}}$ in g/cm^2 vs. Energy in $\text{Log}_{10}(\text{eV})$ for the simulated data sets using CONEX with the high energy model QGSJET II.4, for the energy range of the data, between $10^{18.2}$ and $10^{19.0}$ eV. The circle points are the $\lambda_{p\text{-air}}$ values obtained from the X_0 distribution. Triangle points are the ones determined from reconstructing the $\lambda_{p\text{-air}}$ values using the K -Factor method.

The K value is dependent on the high energy model used. The obtained K value is shown using CONEX 6.4 in Table I, together with the corresponding inelastic proton-air cross section $\sigma_{p\text{-air}}^{\text{inel}}$. Note that, the $\sigma_{p\text{-air}}^{\text{inel}}$ is calculated using equation 5 with Λ_m obtained from the TA X_{\max} distribution and K tabulated for each the high energy models QGSJET II.4 [37, 38], QGSJET01 [39], SIBYLL2.3 [34, 35], and EPOS-LHC [36].

Each K listed in Table I is the average value of K over

the energy range of $10^{18.2}$ - $10^{19.0}$ eV. The value of K is measured to be $\sim 20\%$ larger than 1.0 meaning the slope of the tail of the X_{\max} distribution falls more slowly than the X_0 tail. This is because the X_{\max} distribution resembles a convolution of a falling exponential, from the contribution of X_0 , and a Gaussian from the growth of the shower and fluctuations of stochastic processes of shower development [45]. Showers exhibit large intrinsic fluctuations in development even for those initiated by particles of the same mass and energy. If showers did not exhibit these fluctuations, air shower X_{\max} distributions would resemble the distribution of X_0 , just shifted to a greater depth in the atmosphere by a constant amount. It is important to note that the K value model dependence shown in Table I is on the order of $\sim \pm 3\%$ (K -Value historical improvement is discussed in [23]). This makes the K -Value method weakly model dependent and thus a reliable method to use in calculating the $\sigma_{p\text{-air}}^{\text{inel}}$.

Model	K	$\sigma_{p\text{-air}}^{\text{inel}}$ (mb)
QGSJET II.4	1.17 ± 0.01	505.4 ± 34.8
QGSJET01	1.19 ± 0.01	514.1 ± 35.4
SIBYLL2.3	1.24 ± 0.01	535.6 ± 36.9
EPOS-LHC	1.22 ± 0.01	527.0 ± 36.3

TABLE I. The value of K obtained for each of the high energy models and the corresponding inelastic proton-air cross section for that model. Each K listed is the single average value of K over the energy range of $10^{18.2}$ - $10^{19.0}$ eV. Note that the values of K shows a $\sim \pm 3\%$ model uncertainty.

In order to quantify the systematic uncertainties in the $\sigma_{p\text{-air}}^{\text{inel}}$ measurement, several checks were applied. First, systematic uncertainty due to model dependence is reported. This is done by quantifying the maximum variation in the $\sigma_{p\text{-air}}^{\text{inel}}$ value by each model from the average $\sigma_{p\text{-air}}^{\text{inel}}$ obtained from all of the high energy models. This uncertainty was found to be equal to ± 15 mb.

In addition, the systematic effect of possible energy dependent bias in the X_{\max} distribution was studied. This was done by shifting the values of X_{\max} by their elongation rate (the rate of change of shower $\langle X_{\max} \rangle$ w.r.t. shower energy) prior to fitting. The systematic effect from a possible energy bias was found to be negligible.

The systematic effects due to detector bias is also tested. This systematic effect is done by comparing the attenuation length calculated with and without detector effects. First, the attenuation length is calculated from simulations, where the detector effect is not included. After which, Λ_m is calculated from simulation, where the events are propagated through the detector, reconstructed, and the quality cuts applied. The value of Λ_m was found to be consistent, for all the high energy models, between the thrown events and the reconstructed events with quality cuts applied. Therefore, the systematic effect from this test was found to be negligible. For further details concerning this test procedure refer to [23].

Another systematic check is done by studying the impact of contamination from other primaries. The systematic effect of other elements in the tail beside proton including photon, CNO, helium and iron is investigated. Only photons and helium introduce a bias in the inelastic proton-air cross section.

The upper limit of cosmic-ray photon fraction at the energy range in this study is found to be $\sim 1.0\%$, which is the best upper limit in the Northern hemisphere reported from the Yakutsk air-shower array [46]. The systematic uncertainty due to 1.0% gamma contamination is found to be $+20$ mb. The contamination of helium in Telescope Array data between $10^{18.2}$ - $10^{19.0}$ eV is measured to not larger than 43.8% at the 95% c.l. Using this limit, the systematic uncertainty due to helium contamination is found to be -40 mb.

Note here that the sign for the systematic uncertainty due to helium and gamma contamination is negative and positive respectively. Helium has a larger cross-section than protons. Therefore, helium contamination will result in the observation of a larger cross section than would be the case with pure protons. The opposite occurs due to gamma contamination. The final systematic uncertainty for the $\sigma_{p\text{-air}}^{\text{inel}}$ is calculated by adding each of the systematic uncertainties quadratically.

The final proton-air cross section measured by the Telescope Array detector at an average energy of $10^{18.45}$ eV using the K -Factor method and including the statistical and systematic checks is $\sigma_{p\text{-air}}^{\text{inel}} = 520.1 \pm 35.8$ [Stat.] $^{+25}_{-40}$ [Sys.] mb. This result is shown in Figure 9 and is compared to other experimental measurements [15–23] and current high energy model predictions. Note here that the current proton-air cross section result including the error fluctuations is consistent with the high energy models tuned to the LHC (QGSJET II.4 [37, 38], SIBYLL 2.3 [34, 35], and EPOS-LHC [36]) shown in Figure 9.

C. Proton-Proton Cross Section

The analysis to convert from the inelastic proton-air cross section to proton-proton cross section consists of two parts.

The first part is done by converting the measured inelastic proton-air cross section to the possible allowed values of the proton-proton cross. The conversion is obtained using the Glauber formalism [24] which gives $\sigma_{p\text{-air}}^{\text{inel}}$ as a function of σ_{pp}^{tot} and B , where B is the forward scattering elastic slope. The three curved lines in Figure 10 show the TA measurement of $\sigma_{p\text{-air}}^{\text{inel}}$ and its statistical uncertainties allowed region in the $(\sigma_{pp}^{\text{tot}}-B)$ plane.

The second part is done by constraining the relation between σ_{pp}^{tot} and B using a theoretical model. The model used in this work is (Block, Halzen, and Stanev (BHS)) [25], shown as the dashed line in Figure 10. The intersection of the $\sigma_{p\text{-air}}^{\text{inel}}$ allowed region and the theoretical constraint (BHS model) gives us σ_{pp}^{tot} and B values.

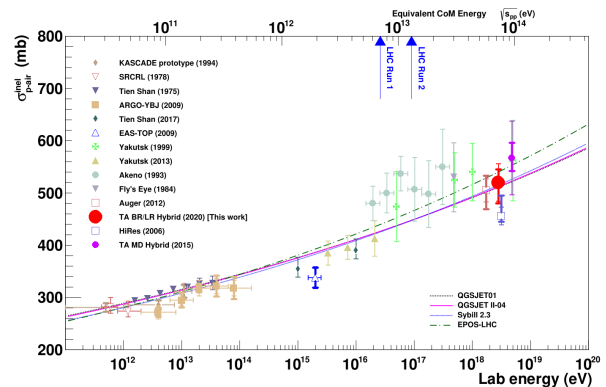


FIG. 9. The proton-air cross section result of this work, including the statistical (thin) and systematics (thick) error bars, in comparison to previous experimental results [15–23]. In addition, the high energy models (QGSJET II.4, QGSJET01, SIBYLL 2.3, EPOS-LHC) cross section predictions are shown.

Note that the BHS model can be replaced with other models or predictions to solve for the σ_{pp}^{tot} . Note the BHS model is consistent with the unitarity constraint while describing the pp and $\bar{p}p$ cross section data from the Tevatron well [47, 48].

The proton-proton cross section in this work is found to be $\sigma_{pp}^{\text{tot}} = 139.4^{+23.4}_{-21.3}$ [Stat.] $^{+15.0}_{-24.0}$ [Sys.] mb. This result is shown in Figure 11 in comparison to previously reported values by UHECR experiments [16, 17, 19, 21, 23]. The recent result from LHC by TOTEM at $\sqrt{s} = 7$ and 13 TeV [49, 50] is also shown, in addition to the BHS fit [25]. The best fit of the proton-proton total cross section data by the COMPETE collaboration is also added [51]. For further details concerning the proton-air to proton-proton procedure refer to [23].

V. SUMMARY AND CONCLUSION

Telescope Array has measured the inelastic proton-air cross section of ultra high energy cosmic rays at $\sqrt{s} = 73$ TeV. This measurement is performed for energies that are not accessible to accelerator experiments, therefore provides an important and unique test of standard model predictions about the fundamental nature of matter.

The Telescope Array utilizes a large array of surface detectors and fluorescence telescopes to record the atmospheric depth of maximum size of air showers initiated by

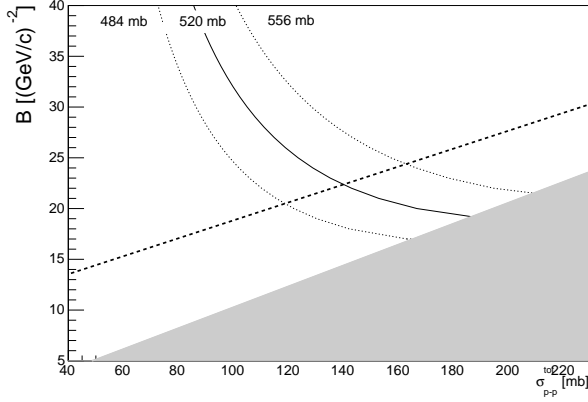


FIG. 10. The elastic slope B in $((\text{GeV}/c)^{-2})$ vs. $\sigma_{p-p}^{\text{total}}$ in mb. The solid line is the allowed $\sigma_{p-p}^{\text{total}}$ values from the $\sigma_{p-p}^{\text{inel}}$ and its statistical errors reported in this work. The dashed line is the BHS fit prediction [52]. While the gray shaded area is the unitarity constraint.

inelastic collisions of ultra high energy cosmic rays and air molecules in the upper atmosphere. By combining the geometric and timing information of SDs and the Black Rock Mesa and Long Ridge FDs that observe a hybrid event X_{max} can be determined with a good precision of $\sim 20 \text{ g/cm}^2$. UHECR X_{max} distributions are related to the interaction length of cosmic rays in the atmosphere, which in turn depends on the tail of X_{max} distributions is populated with the deepest penetrating events, predominantly proton initiated events, the slope of which is related to the interaction length by a constant, K . Using Monte Carlo simulations K can be evaluated using Monte Carlo provides access to the depth of first interaction and X_{max} for each event, allowing a direct determination of K . Once K is known the inelastic proton-air cross section can be determined using equation 5. Using nearly nine years of hybrid data, TA measures $\sigma_{p-\text{air}}^{\text{inel}} = 520.1 \pm 35.8$ [Stat.] $^{+25}_{-40}$ [Sys.] mb for $\sqrt{s} = 73 \text{ TeV}$. Using Glauber theory and the Block, Halzen, Stanev model The total proton-proton cross section is determined from $\sigma_{p-p}^{\text{inel}}$ to be $\sigma_{pp}^{\text{tot}} = 139.4^{+23.4}_{-21.3}$ [Stat.] $^{+15.0}_{-24.0}$ [Sys.] mb.

It is interesting to note that ultra high energy cosmic ray model prediction of the proton-air cross section have converged closer than was the case prior to tuning to LHC data. This is shown in the K value converging from 7% down to 3%. Most importantly, this is also

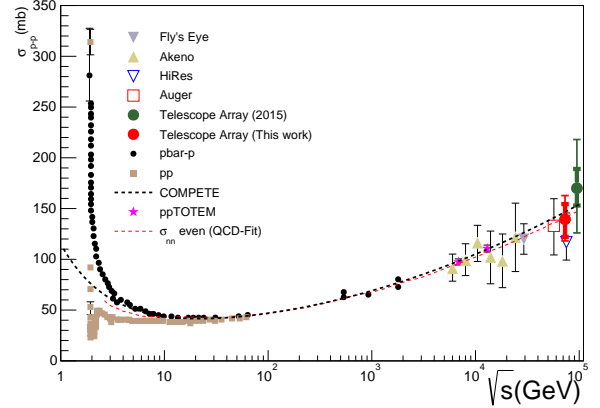


FIG. 11. A compilation of the proton-proton cross section vs. the center of mass energy result of this work, including the statistical (thin) and systematics (thick) error bars, in addition to previous work by cosmic rays detectors [16, 17, 19, 21, 23] in addition to, the recent result from LHC by TOTEM at $\sqrt{s} = 7$ and 13 TeV [49, 50]. The dashed red curve is the BHS fit [25] and the dashed black curve is the fit by the COMPETE collaboration [53]. This plot is adapted and modified from [25].

found to be consistent with results for ultra high energy cosmic ray experiments including this work. The data from the high energy models and ultra high energy cosmic ray experiments continue to show a rising cross section with energy.

Future cross section results, using TA \times 4 [54] will allow us to report on the proton air cross section with greater statistical power. Moreover, including data from the Telescope Array Lower Extension [55] would allow the measurement from 10^{17} – 10^{19} eV with high statistical power and at several energy intervals. This would allow us to make a statement on the functional form of the cross section energy dependence.

VI. ACKNOWLEDGEMENTS

The Telescope Array experiment is supported by the Japan Society for the Promotion of Science (JSPS) through Grants-in-Aid for Priority Area 431, for Specially Promoted Research JP21000002, for Scientific Research (S) JP19104006, for Specially Promoted Research JP15H05693, for Scientific Research

(S) JP15H05741, for Science Research (A) JP18H03705, for Young Scientists (A) JPH26707011, and for Fostering Joint International Research (B) JP19KK0074, by the joint research program of the Institute for Cosmic Ray Research (ICRR), The University of Tokyo; by the U.S. National Science Foundation awards PHY-0601915, PHY-1404495, PHY-1404502, and PHY-1607727; by the National Research Foundation of Korea (2016R1A2B4014967, 2016R1A5A1013277, 2017K1A4A3015188, 2017R1A2A1A05071429) ; by the Russian Academy of Sciences, RFBR grant 20-02-00625a (INR), IISN project No. 4.4502.13, and Belgian Science Policy under IUAP VII/37 (ULB). The foundations of Dr. Ezekiel R. and Edna Wattis Dumke, Willard L. Eccles, and George S. and Dolores Doré Eccles all helped with generous donations. The State of Utah supported the project through its Economic Development Board, and the University of Utah through the Office of the Vice

President for Research. The experimental site became available through the cooperation of the Utah School and Institutional Trust Lands Administration (SITLA), U.S. Bureau of Land Management (BLM), and the U.S. Air Force. We appreciate the assistance of the State of Utah and Fillmore offices of the BLM in crafting the Plan of Development for the site. Patrick Shea assisted the collaboration with valuable advice on a variety of topics. The people and the officials of Millard County, Utah have been a source of steadfast and warm support for our work which we greatly appreciate. We are indebted to the Millard County Road Department for their efforts to maintain and clear the roads which get us to our sites. We gratefully acknowledge the contribution from the technical staffs of our home institutions. An allocation of computer time from the Center for High Performance Computing at the University of Utah is gratefully acknowledged.

-
- [1] D. Ivanov, in *36th International Cosmic Ray Conference (ICRC2019)*, International Cosmic Ray Conference, Vol. 36 (2019) p. 298.
 - [2] T. Abu-Zayyad *et al.* (Telescope Array), *Astrophys. J. Lett.* **768**, L1 (2013), arXiv:1205.5067 [astro-ph.HE].
 - [3] T. Abu-Zayyad *et al.* (Telescope Array), *Astropart. Phys.* **48**, 16 (2013), arXiv:1305.6079 [astro-ph.HE].
 - [4] M. G. Aartsen *et al.* (IceCube), *Phys. Rev.* **D88**, 042004 (2013), arXiv:1307.3795 [astro-ph.HE].
 - [5] R. U. Abbasi *et al.* (HiRes), *Phys. Rev. Lett.* **100**, 101101 (2008), arXiv:astro-ph/0703099 [astro-ph].
 - [6] T. Abu-Zayyad *et al.* (HiRes-MIA), *Astrophys. J.* **557**, 686 (2001), arXiv:astro-ph/0010652 [astro-ph].
 - [7] M. Amenomori, *Adv. Space Res.* **42**, 467 (2008), arXiv:0803.1005 [astro-ph].
 - [8] D. J. Bird *et al.* (HiRes), *Astrophys. J.* **424**, 491 (1994).
 - [9] F. Fenu (Pierre Auger), *PoS ICRC2017*, 486 (2018).
 - [10] J. W. Fowler, L. F. Fortson, C. C. H. Jui, D. B. Kieda, R. A. Ong, C. L. Pryke, and P. Sommers, *Astropart. Phys.* **15**, 49 (2001), arXiv:astro-ph/0003190 [astro-ph].
 - [11] D. Ivanov, *Proceedings, 34th International Cosmic Ray Conference (ICRC 2015): The Hague, The Netherlands, July 30-August 6, 2015*, *PoS ICRC2015*, 349 (2016).
 - [12] S. Knurenko, I. Petrov, Z. Petrov, and I. Sleptsov, *Proceedings, 18th International Symposium on Very High Energy Cosmic Ray Interactions (ISVHECRI 2014): Geneva, Switzerland, August 18-22, 2014*, *EPJ Web Conf.* **99**, 04001 (2015).
 - [13] M. Nagano, M. Teshima, Y. Matsubara, H. Y. Dai, T. Hara, N. Hayashida, M. Honda, H. Ohoka, and S. Yoshida, *J. Phys.* **G18**, 423 (1992).
 - [14] V. V. Prosin *et al.*, *Proceedings, 18th International Symposium on Very High Energy Cosmic Ray Interactions (ISVHECRI 2014): Geneva, Switzerland, August 18-22, 2014*, *EPJ Web Conf.* **99**, 04002 (2015).
 - [15] F. Siohan, R. Ellsworth, A. Ito, J. Macfall, R. Streitmatter, *et al.*, *J. Phys.* **G4**, 1169 (1978).
 - [16] R. Baltrusaitis, G. Cassidy, J. Elbert, P. Gerhardy, S. Ko, *et al.*, *Phys.Rev.Lett.* **52**, 1380 (1984).
 - [17] M. Honda, M. Nagano, S. Tonwar, K. Kasahara, T. Hara, *et al.*, *Phys.Rev.Lett.* **70**, 525 (1993).
 - [18] H. Mielke, M. Foeller, J. Engler, and J. Knapp, *J. Phys.* **G20**, 637 (1994).
 - [19] K. Belov (HiRes Collaboration), *Nucl. Phys. Proc. Suppl.* **151**, 197 (2006).
 - [20] G. Aielli *et al.* (ARGO-YBJ Collaboration), *Phys. Rev.* **D80**, 092004 (2009), arXiv:0904.4198 [hep-ex].
 - [21] P. Abreu *et al.* (Pierre Auger Collaboration), *Phys. Rev. Lett.* **109**, 062002 (2012), arXiv:1208.1520 [hep-ex].
 - [22] Aglietta, M. and others (EAS-TOP Collaboration), *Phys. Rev. D* **79**, 032004 (2009).
 - [23] R. U. Abbasi *et al.* (Telescope Array), *Phys. Rev.* **D92**, 032007 (2015), arXiv:1505.01860 [astro-ph.HE].
 - [24] R. Glauber and G. Matthiae, *Nucl. Phys.* **B21**, 135 (1970).
 - [25] M. Block and F. Halzen, *Phys. Rev.* **D72**, 036006 (2005), arXiv:hep-ph/0506031 [hep-ph].
 - [26] T. K. Gaisser and A. M. Hillas, *International Cosmic Ray Conference* **8**, 353 (1977).
 - [27] T. Z. AbuZayyad, *The Energy Spectrum of Ultra High Energy Cosmic Rays*, Ph.D. thesis, Utah U. (2000).
 - [28] H. Tokuno, Y. Tameda, M. Takeda, K. Kadota, D. Ikeda, *et al.*, *Nucl. Instrum. Meth.* **A676**, 54 (2012), arXiv:1201.0002 [astro-ph.IM].
 - [29] Y. Tameda *et al.*, *Nucl. Instrum. Meth.* **A609**, 227 (2009).
 - [30] T. Abu-Zayyad *et al.* (Telescope Array), *Nucl. Instrum. Meth.* **A689**, 87 (2013), arXiv:1201.4964 [astro-ph.IM].
 - [31] R. U. Abbasi *et al.* (Telescope Array), *Astrophys. J.* **858**, 76 (2018), arXiv:1801.09784 [astro-ph.HE].
 - [32] R. Ulrich, J. Blumer, R. Engel, F. Schussler, and M. Unger, *New J. Phys.* **11**, 065018 (2009), arXiv:0903.0404 [astro-ph.HE].
 - [33] D. Heck, G. Schatz, T. Thouw, J. Knapp, and J. Capdevielle, (1998).
 - [34] R. Fletcher, T. Gaisser, P. Lipari, and T. Stanev, *Phys. Rev.* **D50**, 5710 (1994).

- [35] E.-J. Ahn, R. Engel, T. K. Gaisser, P. Lipari, and T. Stanev, Phys. Rev. D **80**, 094003 (2009), arXiv:0906.4113 [hep-ph].
- [36] T. Pierog, I. Karpenko, J. M. Katzy, E. Yatsenko, and K. Werner, Phys. Rev. **C92**, 034906 (2015), arXiv:1306.0121 [hep-ph].
- [37] S. Ostapchenko, *Colliders to cosmic rays. Proceedings, 2nd International Conference, C2CR07, Granlibakken, Lake Tahoe, USA, February 25-March 1, 2007*, AIP Conf. Proc. **928**, 118 (2007), arXiv:0706.3784 [hep-ph].
- [38] S. Ostapchenko, Phys. Rev. **D83**, 014018 (2011), arXiv:1010.1869 [hep-ph].
- [39] N. Kalmykov, S. Ostapchenko, and A. Pavlov, Nucl.Phys.Proc.Suppl. **52B**, 17 (1997).
- [40] R. Engel, D. Heck, and T. Pierog, Ann. Rev. Nucl. Part. Sci. **61**, 467 (2011).
- [41] R. Ulrich, R. Engel, and M. Unger, Phys.Rev. **D83**, 054026 (2011), arXiv:1010.4310 [hep-ph].
- [42] T. Bergmann, R. Engel, D. Heck, N. Kalmykov, S. Ostapchenko, *et al.*, Astropart.Phys. **26**, 420 (2007), arXiv:astro-ph/0606564 [astro-ph].
- [43] T. Pierog *et al.*, Nucl. Phys. Proc. Suppl. **151**, 159 (2006), astro-ph/0411260.
- [44] G. Bossard *et al.*, Phys. Rev. **D63**, 054030 (2001), hep-ph/0009119.
- [45] C. J. Todero Peixoto, V. de Souza, and J. A. Bellido, Astropart. Phys. **47**, 18 (2013), arXiv:1301.5555 [astro-ph.HE].
- [46] A. Glushkov, I. Makarov, M. Pravdin, I. Slepsov, D. Gorbunov, G. Rubtsov, and S. Troitsky, Phys. Rev. D **82**, 041101 (2010), arXiv:0907.0374 [astro-ph.HE].
- [47] J. Dias De Deus, Nucl.Phys. **B59**, 231 (1973).
- [48] A. Buras and J. Dias de Deus, Nucl.Phys. **B71**, 481 (1974).
- [49] G. Antchev *et al.*, EPL **96**, 21002 (2011), arXiv:1110.1395 [hep-ex].
- [50] G. Antchev *et al.* (TOTEM), Eur. Phys. J. **C79**, 103 (2019), arXiv:1712.06153 [hep-ex].
- [51] J. R. Cudell, V. V. Ezhela, P. Gauron, K. Kang, Yu. V. Kuyanov, S. B. Lugovsky, E. Martynov, B. Nicolescu, E. A. Razuvaev, and N. P. Tkachenko (COMPETE), Phys. Rev. Lett. **89**, 201801 (2002), arXiv:hep-ph/0206172 [hep-ph].
- [52] M. Block, F. Halzen, and T. Stanev, Phys.Rev. **D62**, 077501 (2000), arXiv:hep-ph/0004232 [hep-ph].
- [53] J. R. Cudell, V. V. Ezhela, P. Gauron, K. Kang, Y. V. Kuyanov, S. B. Lugovsky, E. Martynov, B. Nicolescu, E. A. Razuvaev, and N. P. Tkachenko (COMPETE Collaboration), Phys. Rev. Lett. **89**, 201801 (2002).
- [54] E. Kido, in *European Physical Journal Web of Conferences*, European Physical Journal Web of Conferences, Vol. 210 (2019) p. 06001.
- [55] R. U. Abbasi *et al.* (Telescope Array), Astrophys. J. **865**, 74 (2018), arXiv:1803.01288 [astro-ph.HE].